Supplementary Information

Light Radiation Annealing Enables Unidirectional Crystallization of Vacuum-Assisted Sn-Pb Perovskite for Efficient Tandem Solar Cells

Ciyu Ge[a], Qi Xu[a], Dayu Liu[a], Wenjiang Ye[a], Yongxin Zhu[a], Peiyan Zhang[a], Jiakuan Yang[b], Guangxing Liang[c], Ling Xu[a], Ying Zhou[a,d], Haisheng Song[a], Chao Chen[a,d,e]*, Jiang Tang[a,d,e]*

[a] Wuhan National Laboratory for Optoelectronics (WNLO) and School of Optical and Electronic Information (SOEI), Huazhong University of Science and Technology, Wuhan, 430074, China.

[b] School of Environmental Science and Engineering, Huazhong University of Science and Technology, Wuhan, 430074, China.

[c] State Key Laboratory of Radio Frequency Heterogeneous Integration College of Physics and Optoelectronic Engineering, Shenzhen University, Shenzhen, 518060, China.

[d] Hubei Optical Fundamental Research Center, Wuhan, 430074, China.

[e] Optics Valley Laboratory, Wuhan, 430074, China.

* Corresponding author. Email: jtang@mail.hust.edu.cn, cchen@hust.edu.cn

Supplementary Note 1

Based on attenuation law, the penetration depth of X-rays, z, in perovskite materials can be calculated according to the Equation (S1)[1],

$$z = \frac{1}{\mu}\left(\frac{1}{sin\alpha_i} + \frac{1}{\sin(2\theta - \alpha_i)}\right)^{-1} \quad \text{(S1)}$$

where α_i is the incidence angle, 2θ is the Bragg angle and μ is the attenuation coefficient. For narrow-bandgap $Cs_{0.1}FA_{0.6}MA_{0.3}Sn_{0.5}Pb_{0.5}I_3$ perovskite, μ is 284.5 under 8 keV acceleration. The penetration depths for different incidence angles were calculated according to Equation (S1) and presented in Figure S2a.

Supplementary Note 2

The radiative limit of the QFLS can be calculated with the following Equation (S2)[2],

$$QFLS = k_B T \cdot \ln\left(PLQY \frac{J_G}{J_{rad,0}}\right) \quad \text{(S2)}$$

where k_B is the Boltzmann constant, T is the temperature $J_{rad,0}$ is the dark radiative recombination current and J_G is the generation current under illumination. Using Equation S2 and the PLQY, we determined that the QFLS of the HPA-based Sn-Pb PSCs is 0.8874 V, which is approximately 20 mV lower than the LRA-based Sn-Pb PSCs (0.9055 V).

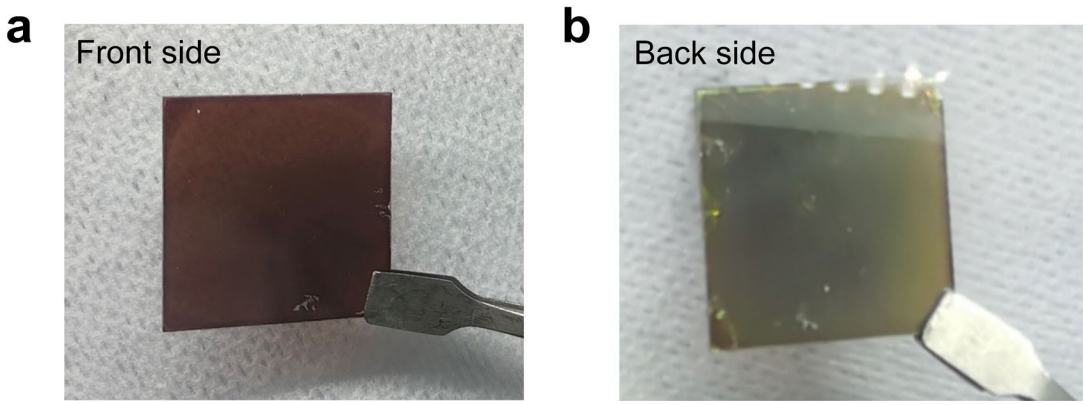

Figure S1. (a) Photograph of the front side of Sn-Pb perovskite films after vacuum-assisted extraction, where a brown-black film can be observed. (b) Photograph of the back side of Sn-Pb perovskite films after vacuum-assisted extraction, where yellow solvent residues are visible. From the front side and back side photographs, it can be observed that a perovskite thin film has already formed on the upper layer, while a significant amount of free solvent remains unextracted at the bottom buried interface.

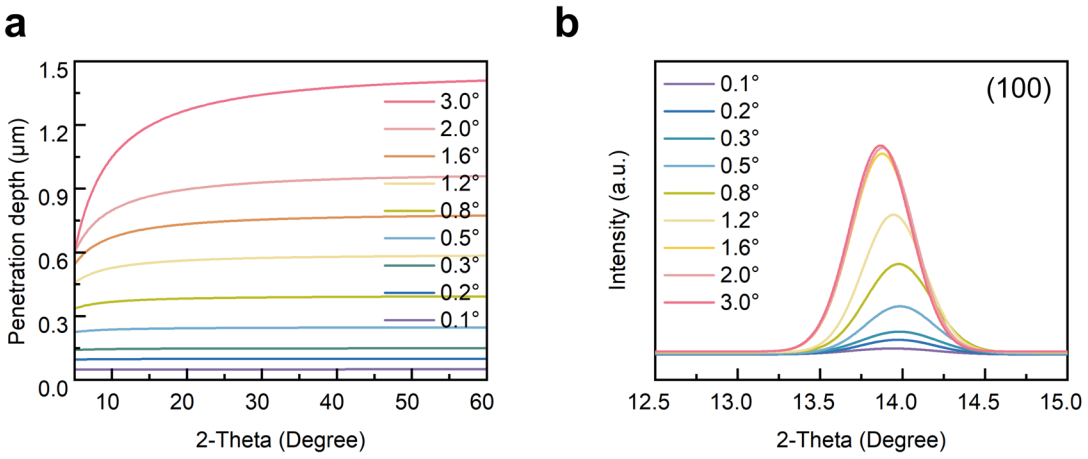

Figure S2. (a) Calculated X-ray penetration depths for different grazing incidence angles for $Cs_{0.1}FA_{0.6}MA_{0.3}Pb_{0.5}Sn_{0.5}I_3$ perovskite. (b) Variable GIXRD spectra of Sn-Pb perovskite film before annealing. The GIXRD intensity increases as the incidence angle changes from 0.1° to 1.6°. Beyond an incidence angle of 1.6°, the GIXRD intensity reaches saturation. This indicates that the upper side of the annealed film has formed perovskite crystals with preferred orientation, while the lower layer has not undergone crystallization.

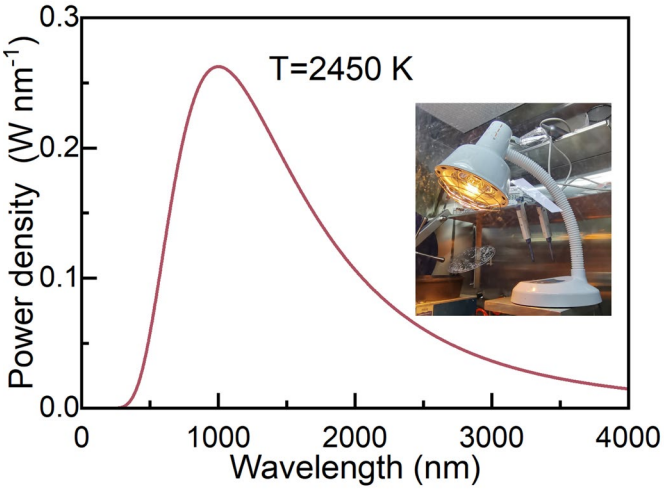

Figure S3. Spectral heat distribution diagram of light radiation sources. The radiation from the light source complies with the blackbody radiation law.

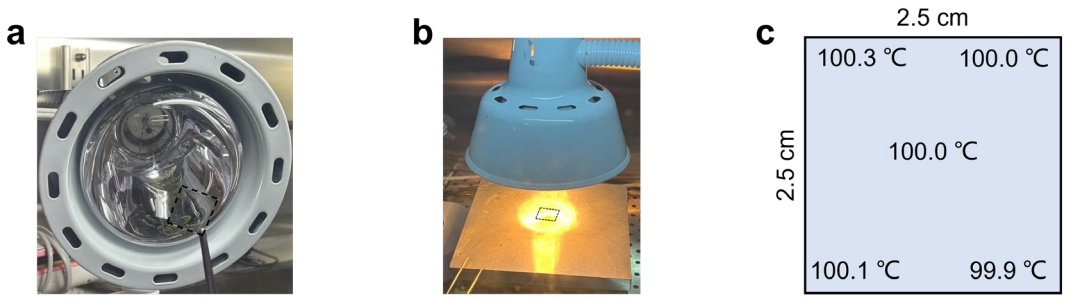

Figure S4. (a) The photograph of the glass substrate (2.5 cm×2.5 cm) and the lamp (the dimeter is 12.5 cm). (b)The photograph of the actual LRA process. (c)The temperatures at different positions on the glass substrate during LRA process.

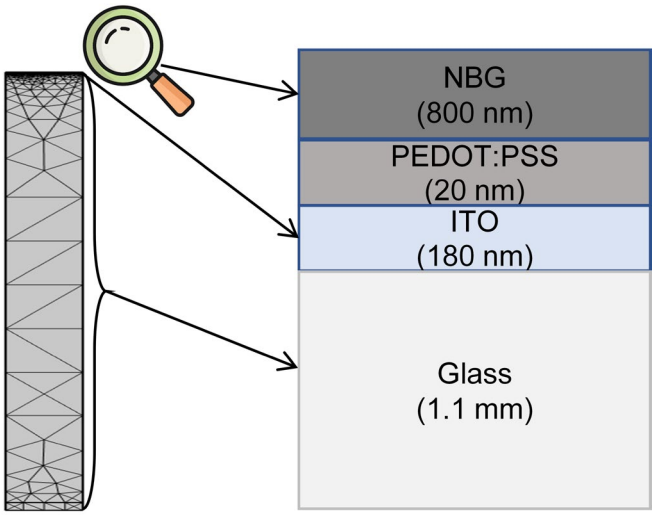

Figure S5. Meshing and device structure in COMSOL simulation. From bottom to top, the layers are arranged as follows: glass (1.1 mm), ITO (180 nm), PEDOT:PSS (20 nm) and NBG film (800 nm).

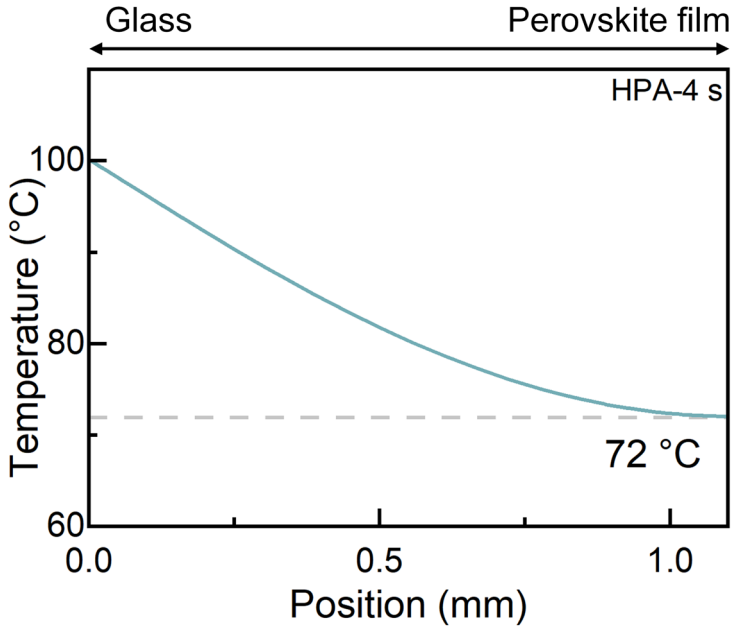

Figure S6. Temperature at different positions during 4 s of HPA. The bottom surface of the glass has reached 100 °C, while the upper surface of the perovskite film is only 72 °C.

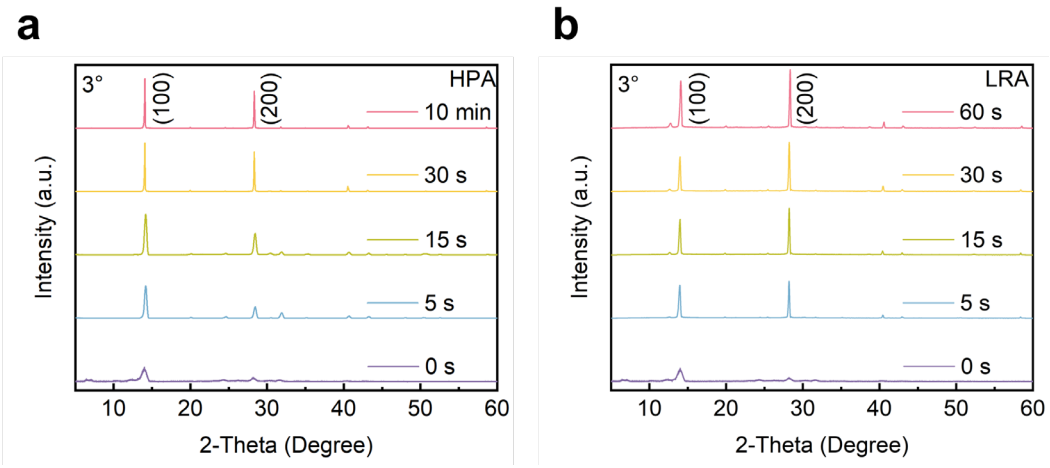

Figure S7. The XRD spectra of Sn-Pb perovskite film under (a) HPA and (b) LRA processes.

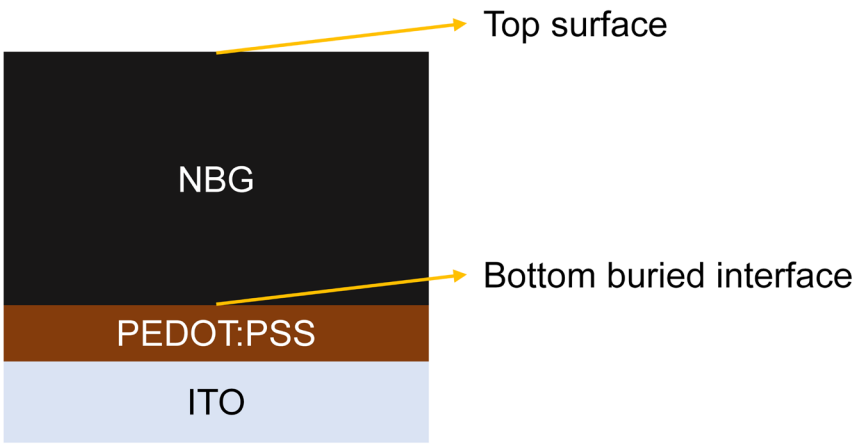

Figure S8. Schematic diagram of the top surface and bottom buried interface of the sample.

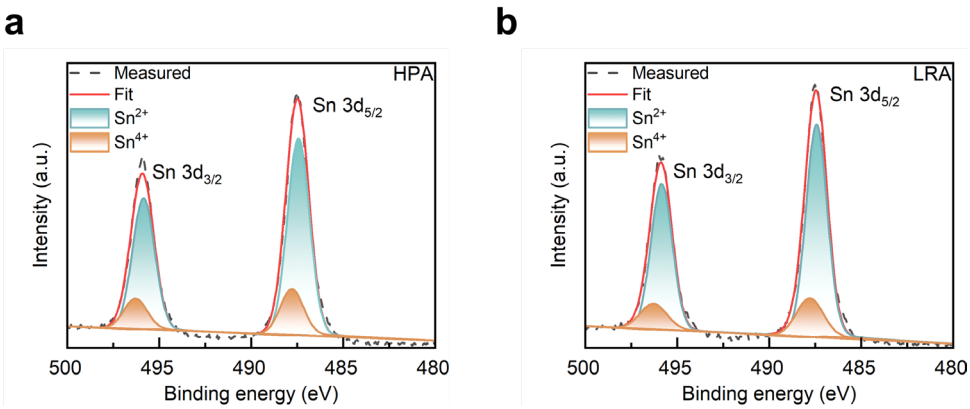

Figure S9. The Sn XPS spectra of Sn-Pb perovskite films under (a) HPA (80.34% Sn^{2+} and 19.66% Sn^{4+}) and (b) LRA (81.81% Sn^{2+} and 18.19% Sn^{4+}).

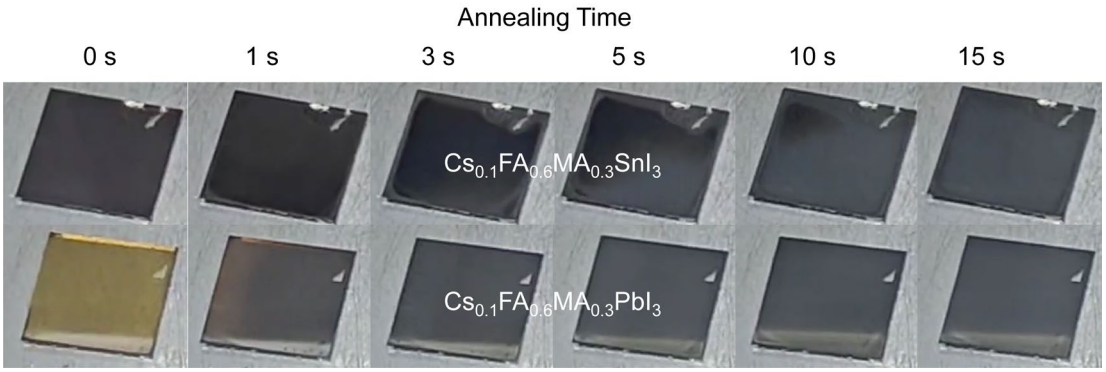

Figure S10. The state changes of different perovskite films under different annealing times. The first row shows the color change during the annealing process of Sn-based perovskite films, which is completed within 15 seconds. The second row shows the color change during the annealing process of Pb-based perovskite films, which is completed within 3 seconds.

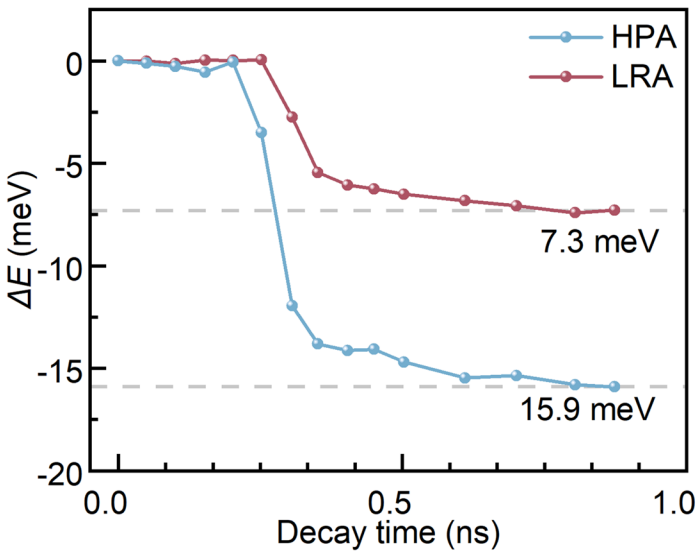

Figure S11. Energy shift of bleaching peak position with decay time. The energy shift for HPA film is 15.9 meV, while the energy shift for LRA film is 7.3 meV.

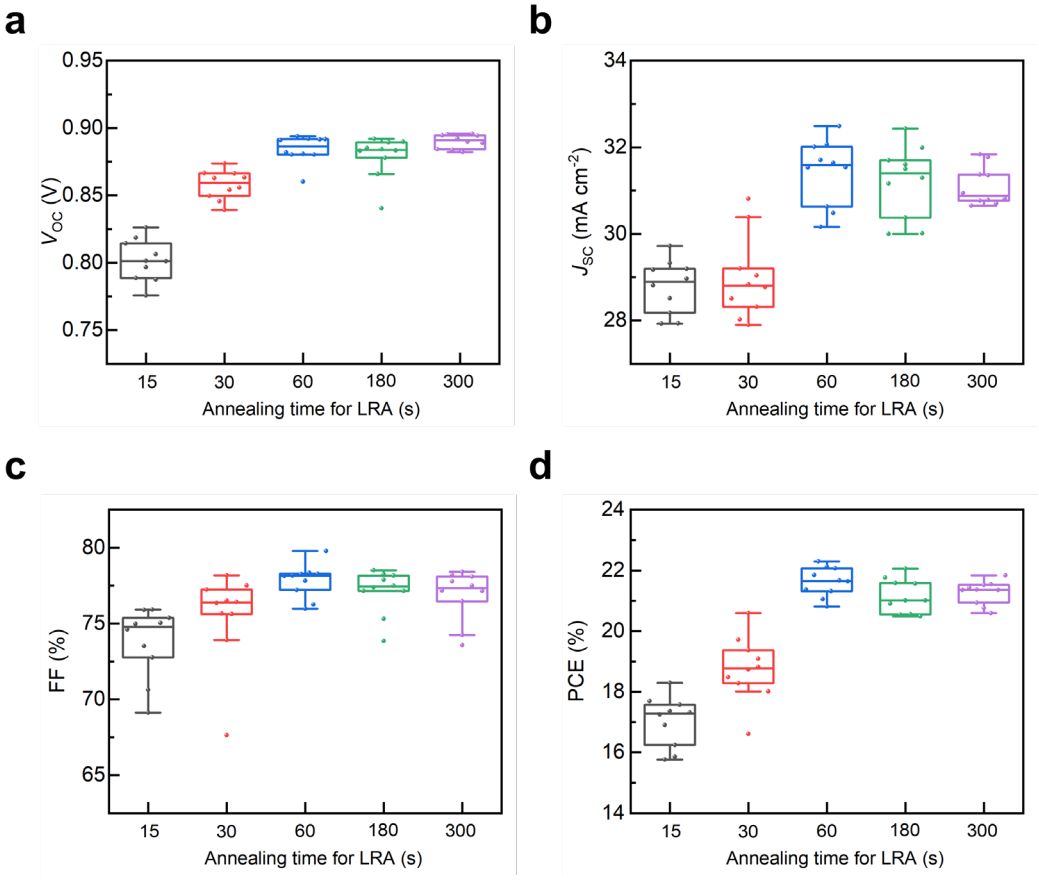

Figure S12. The performance statistics of Sn-Pb PSCs with different LRA times.

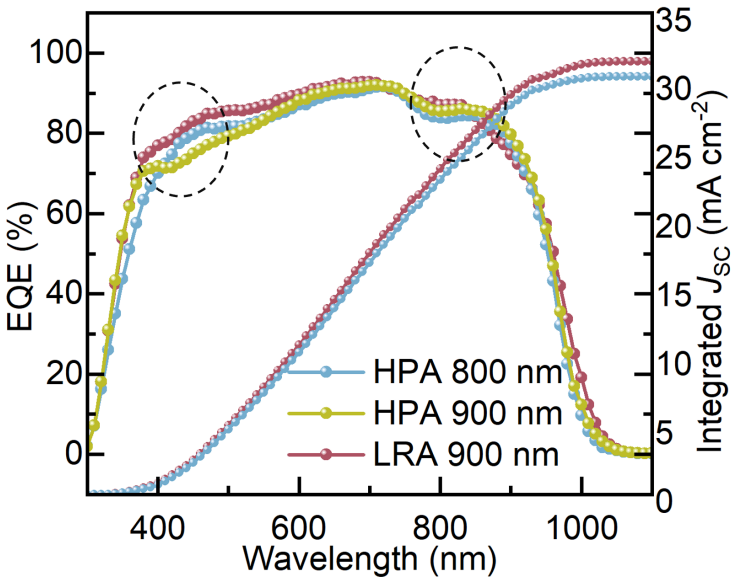

Figure S13. EQE spectra of Sn-Pb PSCs with different film thickness. The *J*sc values from the EQE spectra for 800 nm-thickness HPA process, 900 nm-thickness HPA process and 900 nm-thickness LRA process are 30.39, 30.67and 31.48 mA cm^{-2}, respectively.

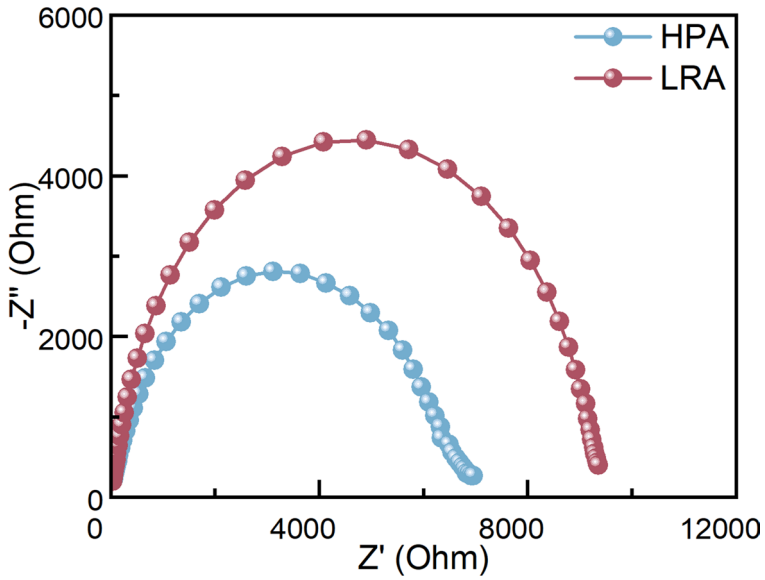

Figure S14. The EIS diagrams of Sn-Pb PSCs under different annealing conditions. The EIS diagrams of the LRA device have a larger semicircle corresponding to a larger recombination resistance, indicating a lower charge recombination rate compared to the HPA device.

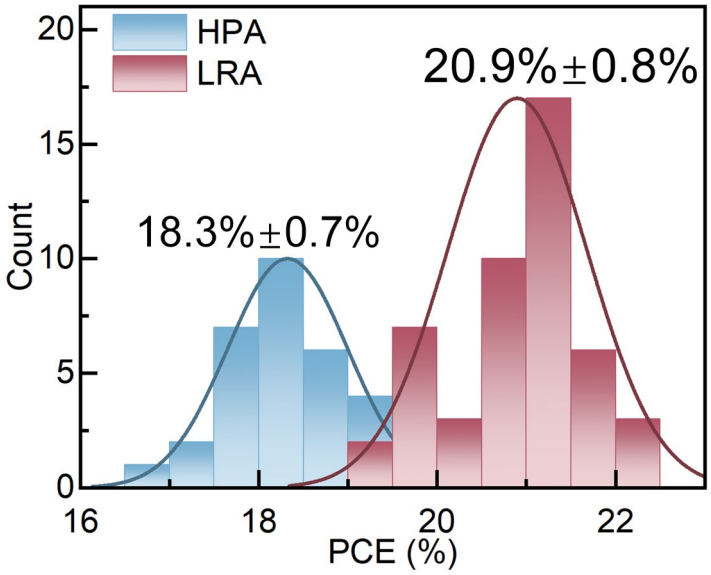

Figure S15. The efficiencies statistical chart of 32 HPA and 48 LRA Sn-Pb PSCs.

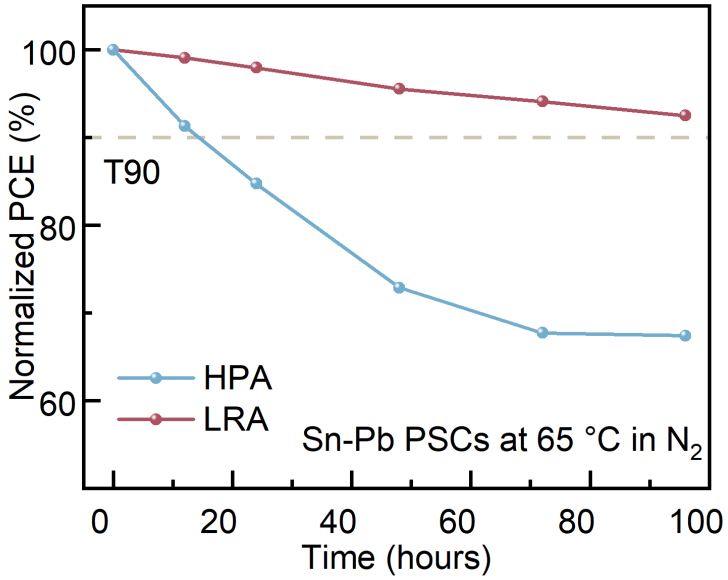

Figure S16. Thermal stability of HPA and LRA Sn-Pb PSCs.

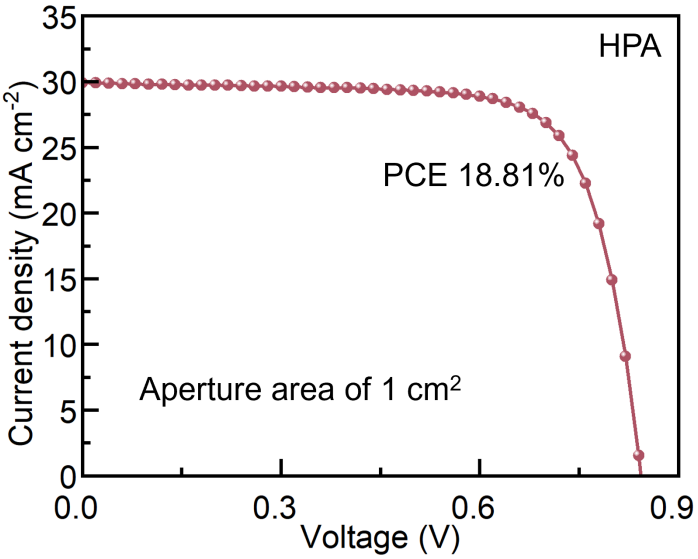

Figure S17. *J-V* curves of 1-cm^2 HPA Sn-Pb PSC.

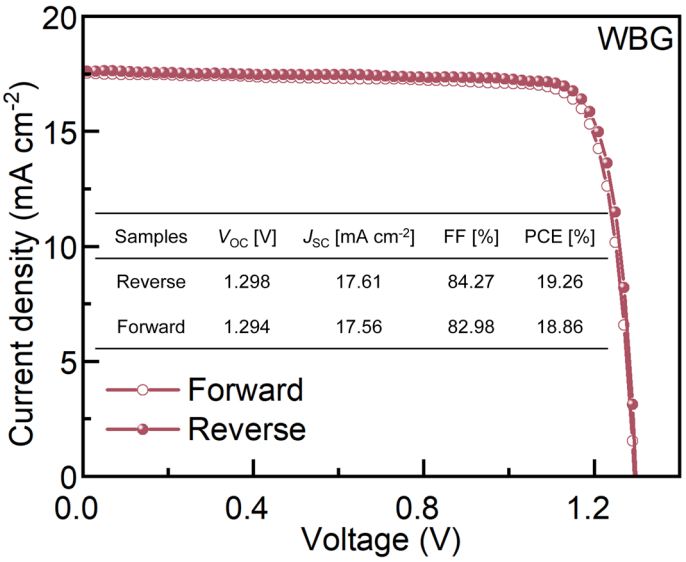

Samples	V_{OC} [V]	J_{SC} [mA cm^{-2}]	FF [%]	PCE [%]
Reverse	1.298	17.61	84.27	19.26
Forward	1.294	17.56	82.98	18.86

Figure S18. *J-V* curves of WBG PSCs under AM 1.5G solar illumination.

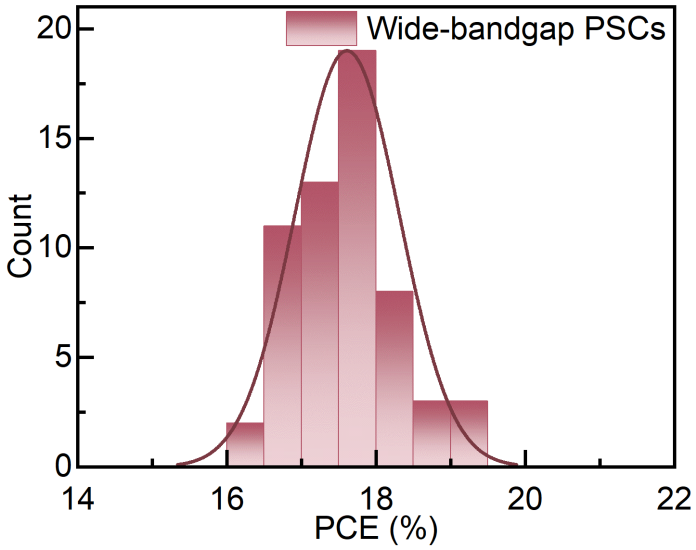

Figure S19. The efficiencies statistical chart of wide-bandgap PSCs.

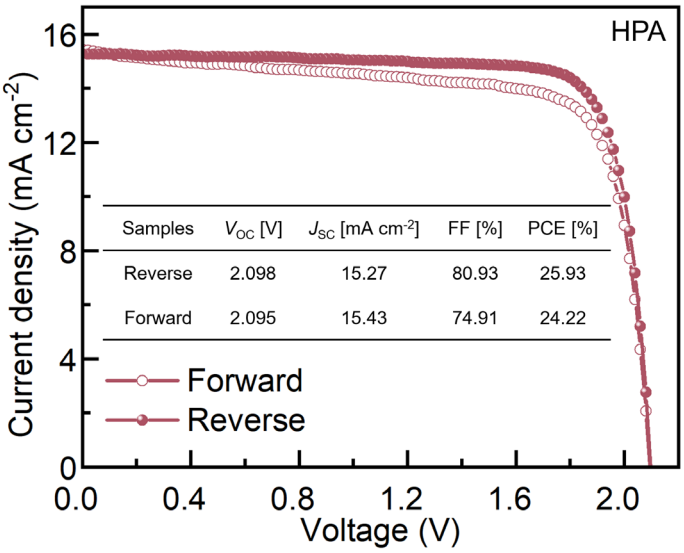

Figure S20. *J-V* curves of all-perovskite tandem solar cells fabricated by the HPA method.

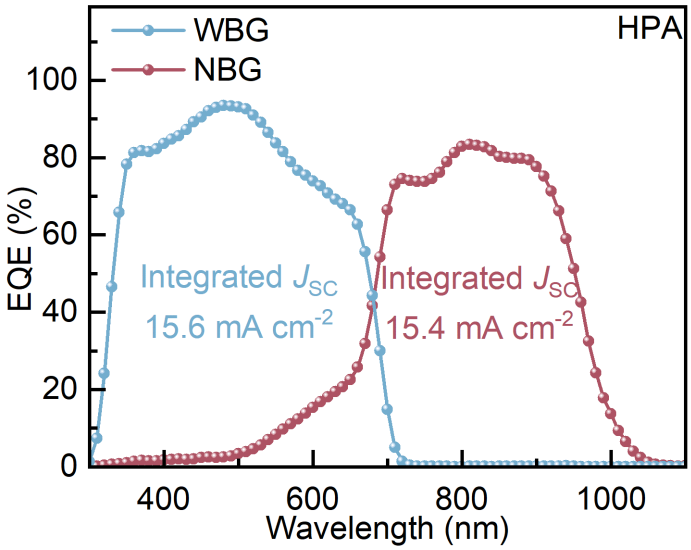

Figure S21. EQE spectra of the bottom and top subcells fabricated by the HPA method.

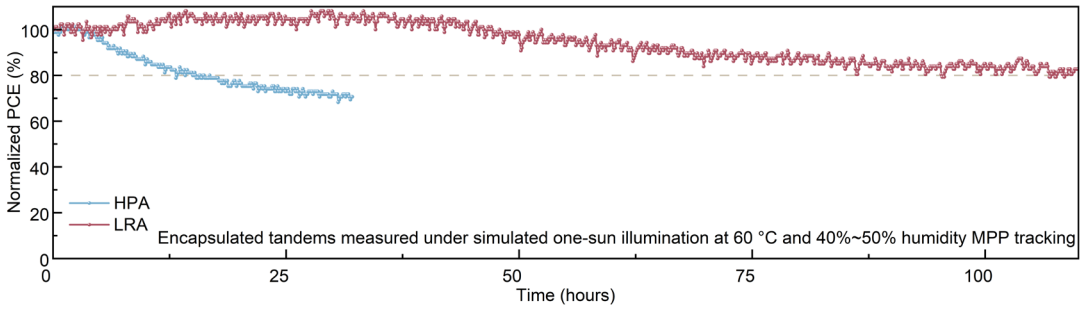

Figure S22. MPP tracking results of the HPA and LRA tandems measured under a white LED solar simulator with simulated one-sum illumination.

Table S1. Parameters of the tungsten filament lamp

Parameter	Value
Power	375 W
Intensity	~500W/m^2
Wavelength range	0.76-4 μm
Lamp head diameter	125 mm

Table S2. Key thermal parameters for COMSOL simulation[3]

Parameter	Unit	Glass	ITO	PEDOT:PSS	Perovskite
Thickness	μm	1100	0.18	0.02	0.8
Density	g cm^{-3}	2.4	6.4	1.2	4
Thermal conductivity	W m^{-1} K^{-1}	0.6	0.4	0.3	1
Heat capacity	J g^{-1} K^{-1}	0.7	0.4	0.2	0.5

Table S3. Fitting parameters for TRPL curves of Sn-Pb perovskite films

Samples	τ_{ave} (ns)	τ_1 (ns)	τ_2 (ns)	$A1$ (%)	$A2$ (%)
HPA	205.88	21.21	258.58	22.2	77.8
LRA	608.43	206.41	722.48	22.1	77.9

Table S4. PV parameters of LRA all-perovskite tandem solar cells

	V_{OC} [V]	J_{SC} [mA cm^{-2}]	FF [%]	PCE [%]
Reverse	2.143	15.98	80.65	27.62
Forward	2.138	15.97	79.39	27.11

Table S5. The efficiency of Sn-Pb PSCs under AM1.5G spectrum in the literature

Year	Extraction Method	V_{OC} [V]	J_{SC} [mA cm^{-2}]	FF [%]	PCE [%]	Ref.
2022	Antisolvent	0.841	33.0	80	22.2	[4]
2023	Antisolvent	0.873	33.0	82.6	23.8	[5]
2023	Antisolvent	0.865	31.59	81.06	22.15	[6]
2024	Antisolvent	0.877	32.19	82.9	23.4	[7]
2024	Antisolvent	0.846	31.4	79.5	21.12	[8]
2019	Vacuum-assisted	0.78	24.90	78	15.15	[9]
2020	Vacuum-assisted	0.79	28.42	78	17.51	[10]
2020	Vacuum-assisted	0.81	30.0	75	18.2	[11]
2022	Gas-assisted	0.8	30.2	78.6	19.0	[12]
2022	Vacuum-assisted	0.837	28.53	79.8	19.06	[13]
2022	Gas-assisted	0.859	31.3	75.6	20.3	[14]
2023	Vacuum-assisted	0.8	29.47	75	17.57	[15]
2024	Gas-assisted	0.868	31.47	77.05	21.04	[16]
2024	Gas-assisted	0.856	31.2	80.0	21.4	[17]
2024	**Vacuum-assisted**	**0.889**	**32.47**	**77.26**	**22.31**	**This work**

Reference

1. M. Dimitrievska, A. Fairbrother, R. Gunder, G. Gurieva, H. Xie, E. Saucedo, A. Pérez-Rodríguez, V. Izquierdo-Roca, S. Schorr, *Phys. Chem. Chem. Phys.* 2016, **18**, 8692.

2. P. Caprioglio, J. A. Smith, R. D. J. Oliver, A. Dasgupta, S. Choudhary, M. D. Farrar, A. J. Ramadan, Y.-H. Lin, M. G. Christoforo, J. M. Ball, J. Diekmann, J. Thiesbrummel, K.-A. Zaininger, X. Shen, M. B. Johnston, D. Neher, M. Stolterfoht, H. J. Snaith, *Nat. Commun.* 2023, **14**, 932.

3. T. Ma, Y. An, Z. Yang, Z. Ai, Y. Zhang, C. Wang, X. Li, *Adv. Funct. Mater.* 2023, **33**, 2212596.

4. R. Lin, J. Xu, M. Wei, Y. Wang, Z. Qin, Z. Liu, J. Wu, K. Xiao, B. Chen, S. M. Park, G. Chen, H. R. Atapattu, K. R. Graham, J. Xu, J. Zhu, L. Li, C. Zhang, E. H. Sargent, H. Tan, *Nature* 2022, **603**, 73.

5. R. Lin, Y. Wang, Q. Lu, B. Tang, J. Li, H. Gao, Y. Gao, H. Li, C. Ding, J. Wen, P. Wu, C. Liu, S. Zhao, K. Xiao, Z. Liu, C. Ma, Y. Deng, L. Li, F. Fan, H. Tan, *Nature* 2023, **620**, 994.

6. J. Luo, R. He, H. Lai, C. Chen, J. Zhu, Y. Xu, F. Yao, T. Ma, Y. Luo, Z. Yi, Y. Jiang, Z. Gao, J. Wang, W. Wang, H. Huang, Y. Wang, S. Ren, Q. Lin, C. Wang, F. Fu, D. Zhao, *Adv. Mater.* 2023, **35**, 2300352.

7. S. Tan, C. Li, C. Peng, W. Yan, H. Bu, H. Jiang, F. Yue, L. Zhang, H. Gao, Z. Zhou, *Nat. Commun.* 2024, **15**, 4136.

8. J. Mao, J. Iocozzia, J. Huang, K. Meng, Y. Lai, Z. Lin, *Energy Environ. Sci.* 2018, **11**, 772.

9. L. Zeng, Z. Chen, S. Qiu, J. Hu, C. Li, X. Liu, G. Liang, C. J. Brabec, Y. Mai, F. Guo, *Nano Energy* 2019, **66**, 104099.

10. C. Li, Y. Pan, J. Hu, S. Qiu, C. Zhang, Y. Yang, S. Chen, X. Liu, C. J. Brabec, M. K. Nazeeruddin, Y. Mai, F. Guo, *ACS Energy Lett.* 2020, **5**, 1386.

11. B. Abdollahi Nejand, I. M. Hossain, M. Jakoby, S. Moghadamzadeh, T. Abzieher, S. Gharibzadeh, J. A. Schwenzer, P. Nazari, F. Schackmar, D. Hauschild, L. Weinhardt, U. Lemmer, B. S. Richards, I. A. Howard, U. W. Paetzold, *Adv. Energy Mater.* 2020, **10**, 1902583.

12. K. Xiao, Y.-H. Lin, M. Zhang, R. D. J. Oliver, X. Wang, Z. Liu, X. Luo, J. Li, D. Lai, H. Luo, R. Lin, J. Xu, Y. Hou, H. J. Snaith, H. Tan, *Science* 2022, **376**, 762.

13. H. Lai, J. Hu, X. Zhou, L. Cai, Q. He, C. Chen, Z. Xu, X. Xiao, D. Lan, Y. Mai, F. Guo, *Sol. RRL* 2022, **6**, 2200619.

14. X. Dai, S. Chen, H. Jiao, L. Zhao, K. Wang, Z. Ni, Z. Yu, B. Chen, Y. Gao, J. Huang, *Nat. Energy* 2022, **7**, 923.

15. X. Zhou, H. Lai, T. Huang, C. Chen, Z. Xu, Y. Yang, S. Wu, X. Xiao, L. Chen, C. J. Brabec, Y. Mai, F. Guo, *ACS Energy Lett.* 2023, **8**, 502.

16. C. Ge, B. Jiang, J. Zhu, P. Zhang, R. Ma, S. Yan, Z. Liu, A. Shaker, M. S. Salem, J. Luo, L. Xu, J. Yang, Z. Li, H. Song, C. Chen, J. Tang, *Adv. Funct. Mater.* 2024, 2400075.

17. H. Gao, K. Xiao, R. Lin, S. Zhao, W. Wang, S. Dayneko, C. Duan, C. Ji, H. Sun, A. D. Bui, C. Liu, J. Wen, W. Kong, H. Luo, X. Zheng, Z. Liu, H. Nguyen, J. Xie, L. Li, M. I. Saidaminov, H. Tan, *Science* 2024, **383**, 855.